Journal of Materiomics 11 (2025) 100870

Contents lists available at ScienceDirect

Journal of Materiomics

journal homepage: www.journals.elsevier.com/journal-of-materiomics/

Research paper

A $BaTiO_3$-based flexible ferroelectric capacitor for non-volatile memories

Xingpeng Liu [a], Chunshu Wei [a], Tangyou Sun [a], Fabi Zhang [a], Haiou Li [a], Linsheng Liu [b], Ying Peng [a, *], Hezhang Li [c, **], Min Hong [d, ***]

[a] Guangxi Key Laboratory of Precision Navigation Technology and Application, Guilin University of Electronic Technology, Guilin, 541004, China
[b] School of Electronic and Information Engineering/School of Integrated Circuits, Guangxi Normal University, Guilin, 541004, China
[c] Department of Precision Instrument, Tsinghua University, Beijing, 100084, China
[d] Centre for Future Materials, and School of Engineering, University of Southern Queensland, Springfield Central, Queensland, 4300, Australia

ARTICLE INFO

Article history:
Received 13 January 2024
Received in revised form
2 April 2024
Accepted 7 April 2024
Available online 9 May 2024

Keywords:
$BaTiO_3$ ferroelectric films
Non-volatile memory
Flexible mica substrate

ABSTRACT

$BaTiO_3$ (BTO) ferroelectric films, which are renowned for their lead-free compositions, superior stability, and absence of a wake-up effect, are promising candidate materials in the field of non-volatile memories. However, the prerequisites for high-temperature conditions in the fabrication of ferroelectric thin films impose constraints on the substrate choice, which has limited the advancement in non-volatile memories based on single-crystal flexible BTO films with robust ferroelectric properties. Herein, a technique has been developed for the fabrication of flexible devices using a pulsed laser deposition system. BTO ferroelectric films have then been deposited onto a flexible mica substrate, with $SrTiO_3$ (STO) serving as a buffer layer. The obtained flexible BTO devices exhibited excellent ferroelectricity, with a maximum polarization ($2P_{max}$) of up to 42.58 μC/cm^2 and a remnant polarization ($2P_r$) of up to 21.39 μC/cm^2. Furthermore, even after 1000 bending cycles, the bipolar switching endurance remained high at 10^{12} cycles. After 10^4 s, the flexible BTO device still maintained excellent polarization characteristics. These results make the flexible BTO ferroelectric thin film a potential candidate for the next generation of non-volatile memories.

1. Introduction

The emergence of the interconnected era has increased the need for flexible wearable devices, which in turn requires electronic storage devices with high flexibility, repeatability in bending, and stability [1,2]. Despite notable advancements in the research on rigid substrates, the same progress cannot be directly obtained for flexible storage devices [3–9]. Currently, flexible substrates, such as polyimide (PI) and polydimethylsiloxane (PDMS), have shown lower ferroelectricity and fatigue characteristics [10–13]. The high temperatures that are required for thin film growth limit the application of these polymer substrates [14–16]. To address this challenge, the method of sacrificial layer etching has been proposed as a solution to transfer ferroelectric thin films [14,17–24]. However, the small size of the transferred film and the complexity of this method have become additional challenges. Mica, $KAl_2(Si_3AlO_{10})(OH)_2$, which is a layered silicate material with high thermal stability and excellent insulation properties, has emerged as a promising candidate for the growth of ferroelectric thin films [25].

Currently, there are reports on growing $Hf_xZr_{1-x}O$ (HZO) ferroelectric thin films on mica [26–32]. The ferroelectricity of HZO arises from a mixed phase with a non-orthogonal symmetry, which is known as the O-phase [33,34]. This material is highly sensitive to external environmental disturbances, including high temperatures, radiation, and bending stress on flexible substrates. These factors can destabilize the O-phase, which leads to significant wake-up effects and fatigue effects.

In contrast, perovskite thin films (such as $Pb_xZr_{1-x}TiO_3$(PZT), $BiFeO_3$(BFO), $BaTi_xCo_{1-x}O_3$(BTCO), and $Bi_xLa_{1-x}TiO_{12}$(BLT)) on mica [12,16,25,35–42], exhibit ferroelectricity that arises from the displacement of central atoms along the diagonal. This property

* Corresponding author.
** Corresponding author.
*** Corresponding author.
E-mail addresses: pengying@guet.edu.cn (Y. Peng), lihezhang1202@mail.tainghua.edu.cn (H. Li), min.hong@unisq.edu.au (M. Hong).
Peer review under responsibility of The Chinese Ceramic Society.

https://doi.org/10.1016/j.jmat.2024.04.001

allows these materials to maintain excellent polarization characteristics, even in complex environments. However, issues, such as containing toxic Pb element and forming impurity phases like Fe_2O_3, still exist.

$BaTiO_3$ is a lead-free ferroelectric material with a high dielectric constant and low dielectric loss. It has important applications in FeRAMs (ferroelectric random access memories) and ferroelectric tunnel junctions (FTJ). However, there has been limited research on flexible barium titanate (BTO) thin films, while most of previous studies have focused on rigid substrates. Therefore, the preparation of BTO ferroelectric films with high stability and flexibility is crucial for the advancement of non-volatile memory devices. Mica is an excellent substrate in the field of flexible materials, which is due to its unique high-temperature resistance and surface smoothness at the atomic level.

In this study, a pulsed laser deposition system has been used for the fabrication of Pt/BTO/1.1% (in mass) Nb:$SrTiO_3$ (NSTO)/$La_{0.65}Sr_{0.35}MnO_3$(LSMO)/STO thin films on a mica substrate. The high-resolution transmission electron microscopy (HRTEM) analysis revealed well-defined interfaces between the layers of the thin film. Additionally, the BTO ferroelectric thin film showed excellent ferroelectric properties. Notably, the flexible BTO ferroelectric thin film was able to maintain its excellent performance in unbent and bent states, with a high repeatability up to 1000 bending cycles. This study has provided an important method for further research on flexible non-volatile memories.

2. Experimental section

2.1. Sample preparation

Pt/BTO/1.1% (in mass) Nb:$SrTiO_3$ (NSTO)/$La_{0.65}Sr_{0.35}MnO_3$(LSMO)/STO (BTO/NSTO/LSMO/STO) thin films were deposited onto a mica substrate one by one at 750 °C using a pulsed laser deposition system (PLD-S40-L, Beijing Perfect technology Co, Ltd., China), with a 248 nm KrF excimer laser. Prior to deposition, the mica substrate was mechanically stripped to a thickness of 10 μm. Different pressures and laser energies were used when depositing different components. Specifically, the STO films were deposited under an oxygen pressure of 10 Pa and with a laser energy of 330 mJ. The LSMO films were deposited under an oxygen pressure of 30 Pa and with a laser energy of 300 mJ. The Nb:$SrTiO_3$ films were deposited under a vacuum pressure of 1×10^{-4} and with a laser energy of 300 mJ. The BTO films were deposited under an oxygen pressure of 10 Pa and with a laser energy of 300 mJ. Following deposition, these films were annealed for 30 min at 750 °C and then cooled to room temperature at a rate of 7 °C/min. Pt upper electrodes, with a thickness of 60 nm, were deposited on the BTO films using RF magnetron sputtering.

2.2. Structural and electrical characterizations

The phase structure of the BTO/NSTO/LSMO/STO/Mica heterojunctions was analyzed by X-ray diffraction (XRD; Bruker D8 Advance, Germany) with Cu K_α radiation ($\lambda = 1.5405$ Å). The optical transmittance characteristics was investigated by UV−Vis spectroscopy (PerkinElmer Lambda365). The topography of the films was examined using atomic force microscopy (AFM; Bruker MultiMode 8). PIEZORESPONSE force microscopy (PFM) measurements were performed using the Jupiter XR, Oxford Instruments, UK. The surface damage of devices was evaluated by an optical microscope (Nikon eclipse LV150 N). Scanning electron microscopy (SEM; JSM-IT500HR) offered an increased resolution of topographical nuances. Furthermore, the stoichiometry and elemental distribution within the heterojunctions were determined using energy dispersive spectroscopy (EDS; Bruker XFlash 5030) equipped in the transmission electron microscopy (TEM; FEI Tecnai G2 F20).

In addition, the electric transport phenomena through the designed heterojunctions were quantitatively characterized by plotting the *I*−*V* curves using a Keithley 2400 digital source meter. The ferroelectricity, which was an inherent characteristic of the BTO films, was thoroughly quantified using a HUACE FE-2000 Analyzer.

3. Results and discussion

3.1. Structural characterizations

Fig. 1a schematically illustrates the BTO/NSTO/LSMO/STO/Mica multilayer film structure. The crystalline structure of the BTO/NSTO/LSMO/STO/Mica heterojunctions was obtained by XRD (Fig. 1b). The interplanar spacing of BTO ($d_{(111)} = 2.3219$ Å) and STO ($d_{(111)} = 2.2619$ Å) was analyzed and showed 0.34% and 0.39% of the tensile strain, respectively. It is worth noting that the diffraction peak position of the (022)-oriented LSMO was found at 40.077°, with a crystallographic plane spacing, *d*, of 2.2457 Å. This *d* spacing was different from the standard diffraction peak (2.2458 Å) by only 0.0001 Å. The high quality of the epitaxial heterojunction films was confirmed by the minor difference between the actual interplanar spacing and the standard values of STO, LSMO, and BTO. Furthermore, the main crystalline planes were (111) in BTO, (022) in LSMO, and (111) in STO. This was consistent with previous studies that confirmed the epitaxy of (111) planes when BTO, STO, or $CoFe_2O_4$ (CFO) layers were used as buffers [12,16,25,42,43]. To investigate the crystallinity of the films, the half-peak width of BTO (111) was determined to be 1.765° (Fig. S1 Supplemental information). Compared with previous studies, the fabricated flexible BTO films exhibited higher crystallinity [43].

The SEM image revealed the size of flat electrode to be 70 μm × 70 μm (Fig. 1c). The small particles could be interpreted as contaminations induced during SEM sample preparation. Furthermore, the surface morphology of the BTO ferroelectric films was examined using AFM in a 3 μm × 3 μm area, and the results are presented in Fig. 1d. The flexible mica substrate showed an ultra-flat surface with an average surface roughness (R_a) of 0.372 nm and a root mean square roughness (R_{rms}) of 0.294 nm, which ensured an exceptional uniformity of the surface of the film at the atomic scale.

For the optical features, the spectral transmittance of the heterojunction is accurately profiled in Fig. 1e. This was tested without top electrodes. Across the 500−700 nm bandwidth, an examination of the propagation of electromagnetic waves through the material revealed a remarkable transmittance beyond 55%. This was accentuated by a noteworthy peak of 70% at the pivotal wavelength of 503 nm. This notable characteristic of enhanced optical transparency surpassed the achievements of previous research studies, highlighting the exceptional photonic performance of the multilayer films in this study [35].

To investigate the microstructure of the BTO/NSTO/LSMO/STO/Mica heterojunctions, HRTEM analysis of the NSTO/LSMO/STO multilayer buffer film was performed (Fig. 2a). Thicknesses of STO, LSMO, NSTO, and BTO films are around 65, 60, 63 nm, and 260 nm, respectively. The tight connection of the NSTO/LSMO/STO multilayer buffer films provided a solid foundation for the epitaxial growth of BTO. Furthermore, the EDS scans at the cross-sectional interfaces are presented in Fig. 2b−d, revealing uniform elemental distributions of Sr, Mn, and Ti.

HRTEM images along the [111] crystal axis demonstrated the clear interfaces of BTO/NSTO/LSMO/STO/Mica (Fig. 2e−h).

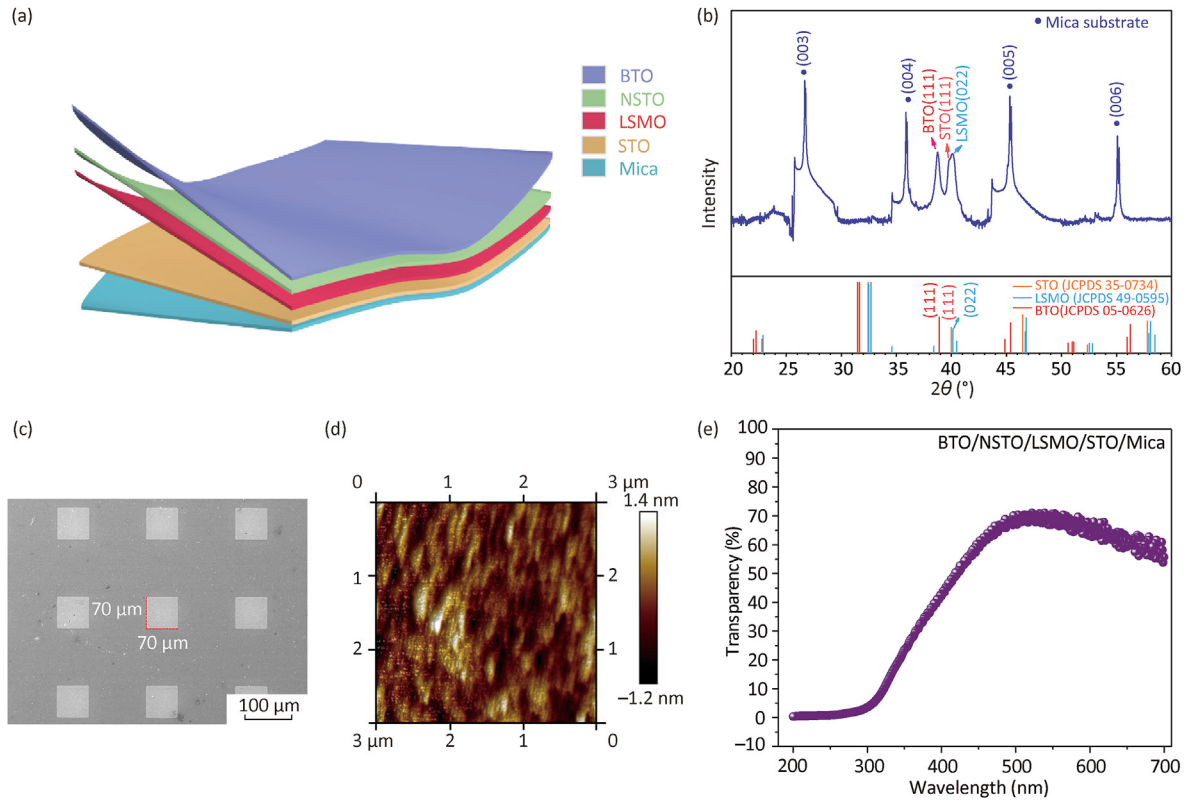

Fig. 1. A BTO/NSTO/LSMO/STO thin film on a mica substrate: (a) schematic diagram of the thin film, (b) XRD patterns, (c) SEM image, (d) AFM image, and (e) transparency examination.

Additionally, the fast Fourier transform (FFT) pattern of STO is presented in the inset of Fig. 2e, along with the corresponding high-resolution TEM image in Fig. 2i. The FFT spectrum showed an equilateral hexagonal shape, which is observed from the [111] zone axis, as shown in Fig. S2 Supplemental information, and the result is similar to previous studie [17]. The FFT pattern confirmed the single crystalline structure of STO. The HRTEM images revealed an interplanar spacing of $d_{sto(110)} = 0.2818$ nm. This was an indication of a high crystalline quality of the buffer layer, which benefited the growth of BTO thin film.

Furthermore, the FFT pattern of the $(\bar{1}21)$ crystal plane of LSMO is presented in Fig. 2f. LSMO was found to be closely arranged with STO at the interface, and no lattice distortions were observed. This confirmed the single crystalline structure in the FFT pattern. HRTEM images of the periodic arrangement of atoms in LSMO are presented in Fig. 2j, with an interplanar spacing, $d_{lsmo(-121)}$, of 0.2803 nm. These results showed the good quality of the single crystal structure in the heteroepitaxial LSMO. Furthermore, there was a significant lattice mismatch between LSMO, BTO, and NSTO, with the corresponding cell edges 3.876, 3.994 Å, and 3.905 Å, respectively. The clear interface between NSTO and LSMO is shown in Fig. 2g, with an FFT pattern that confirms the (110) crystalline plane. This FFT pattern was consistent with the first buffer layer, indicating a good epitaxial growth of the NSTO thin film. The atomic arrangement of NSTO is shown in Fig. 2k, the interplanar spacing of $d_{nsto\ (110)} = 0.2834$ nm is exhibited in HRTEM images, indicating an excellent crystalline quality of the NSTO film.

In addition, the FFT pattern of BTO is presented in Fig. 2h, which also exhibits a single crystalline structure. Its atomic arrangement is presented in Fig. 2l, $d_{bto\ (110)} = 0.2864$ nm is displayed in HRTEM images, with closely bonded neighboring atoms and no atomic dislocation. Thus, a high-quality epitaxial growth of the BTO film had been achieved. Furthermore, the relationship between the lattice spacing of the films that were grown on the mica substrate is shown in Fig. S3 Supplemental information. The measured values of the lattice spacing showed a consistent trend with the reference values, confirming the good epitaxial relationship of the BTO/NSTO/LSMO/STO thin film. Fig. S4 Supplemental information displays the HRTEM and SAED patterns of BTO/NSTO/LSMO/STO/Mica along the [111] zone axis. It further confirmed the epitaxial relationship of the multilayer thin film, which was consistent with the FFT patterns of each layer and the XRD results.

3.2. Ferroelectricity of a flexible BTO film

An optical microscopy image of the flexible Pt/BTO/NSTO/LSMO/STO/Mica device is presented in Fig. 3a. We could observe smooth and flat surface topography across the entire BTO film. Fig. 3b shows current-voltage (I–V) curves of the device. These curves indicated intrinsic memory features of the device. This resistive modulation was attributed to interactions between the charged carriers (such as electrons and positive charges), which moved between the ferroelectric and semiconductor oxide layers in response to the applied electric field. These interactions were ideally translated into modulations of the depletion barrier at the interface, as illustrated in Fig. S5 Supplemental information. When the polarization vectors were oriented towards the lower LSMO electrode, the built-in electric field decreased, which was due to the opposing effect of the external field. This led to a decrease in the Schottky barrier at the BTO/NSTO interface and consequently a reduced resistance (Fig. S5a Supplemental information). On the contrary, the polarization towards the upper Pt electrode caused a displacement of electrons within NSTO, which resulted in a layering of positive charges closer to the depletion layer. The electrons

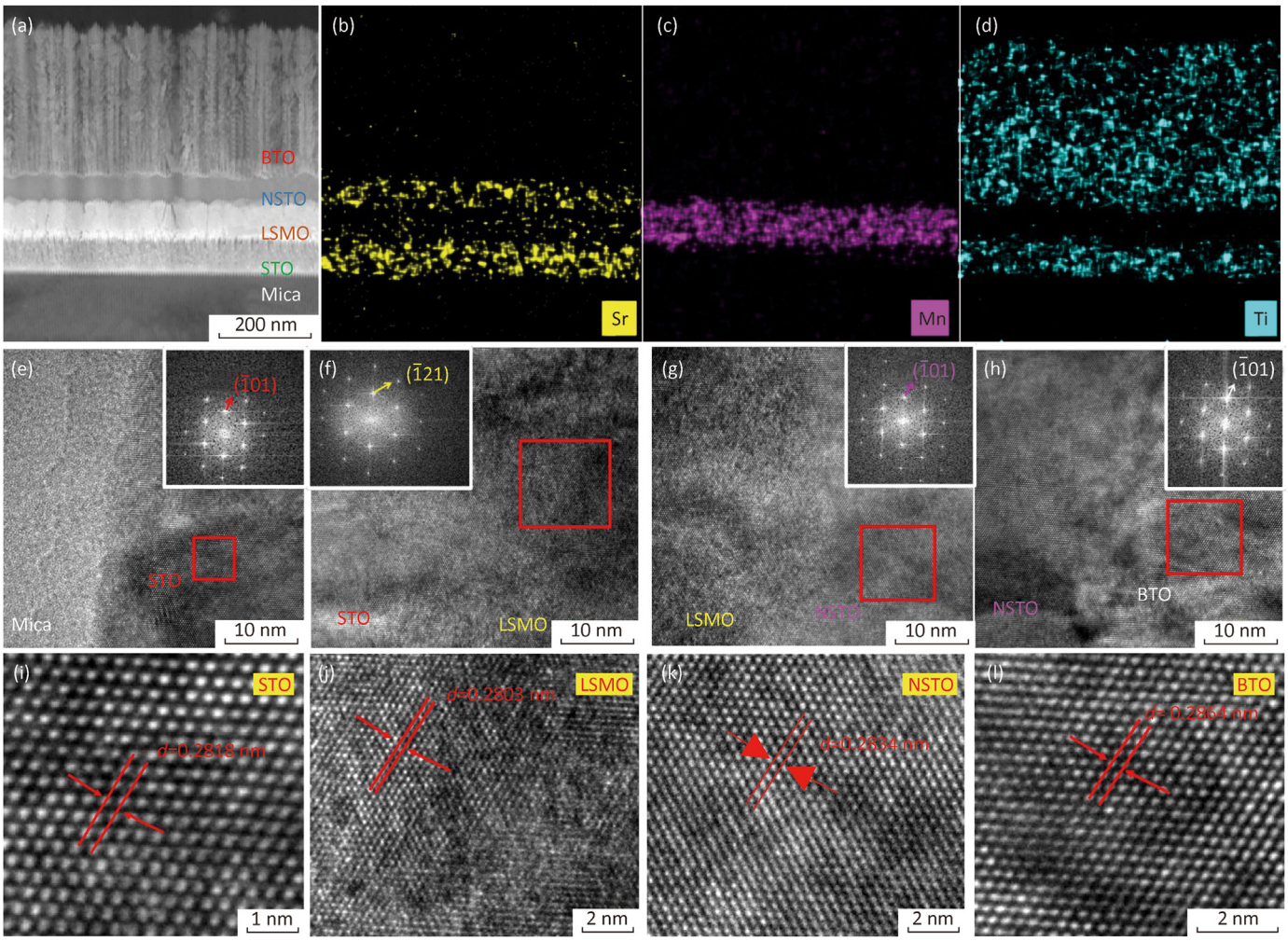

Fig. 2. (a) Cross-sectional TEM image of the BTO/NSTO/LSMO/STO/mica heterostructure. EDS mappings of the (b) Sr, (c) Mn, and (d) Ti elements. HRTEM images with an inset showing the corresponding FFT patterns of the interface areas of (e) STO/mica, (f) LSMO/STO, (g) NSTO/LSMO, and (h) BTO/NSTO. Enlarged HRTEM images of (i) STO, (j) LSMO, (k) NSTO, and (l) BTO, which correspond to the marked areas (in red) in (e)–(h).

within BTO approximated the depletion boundary, which resulted in an enlarged depletion layer and an increased Schottky barrier. This led to a state of increased resistance, as shown in Fig. S5b Supplementary information [44,45].

This difference created two distinctly separated *I*–*V* trajectories at increased voltages. This *I*–*V* curve, with a hysteresis effect, was similar to previous reports [3,46–48]. As can be seen in Fig. S6 Supplementary information, the memristive characteristics of a 7 nm BTO ferroelectric thin film with the same structure has been demonstrated, which has been used to demonstrate the polarization-induced resistance transformation phenomenon. As can also be seen in Figs. S6c and d Supplementary information, the ferroelectric BTO thin film showed a clear switching state, which confirmed the hysteresis effect of the current in Fig. 3b.

To better understand the relationship between the coercive fields and the ferroelectricity, a PFM analysis was used to characterize the polarization properties of the ferroelectric BTO film. Fig. 3c presents the phase diagram of the PFM results. In this diagram, the measured region 3.0 μm × 1.5 μm with +25 V was inserted to the left, and the same range with −25 V was inserted to the right. The reversible ferroelectricity of the BTO thin film was confirmed by a 180° phase difference that was generated between these domains.

The *P*–*V* hysteresis ferroelectric hysteresis loop was tested at 1 kHz for different voltages (Fig. 3d). It was then shown that the *P*–*V* loop was not fully saturated. However, the *P*–*V* loop became saturated for an increased voltage, with a significant increase in the polarization and the coercive field. This could be explained by the redistribution of dipole moments within the ferroelectric material, which was caused by the electric field. Furthermore, the *P*–*V* loop under a reverse bias was close to elliptical, which was due to an increase in leakage current (Fig. S7 Supplementary information). Therefore, a small voltage should be used to prevent a leakage breakdown of the device. Moreover, the flexible Pt/BTO/NSTO/LSMO/STO/Mica device had a maximum polarization, $2P_{max}$, of approximately 42.58 μC/cm^2 and a $2P_r$ residual polarization of about 21.39 μC/cm^2. The values of $2P_r$ and $2P_{max}$ were similar to those of other flexible substrates [49]. Additionally, the flexible device exhibited a coercive field of nearly 245.77 kV/cm when being unbent, which was lower than previously reported values [29,30,50].

Leakage currents, which are fundamental for polarization flips, are presented in Fig. 3e. Two current peaks located near the positive and negative 5 V were then observed, which were caused by a sudden change in the current. This was induced by the external electric field force, which overcame the potential barrier of reverse

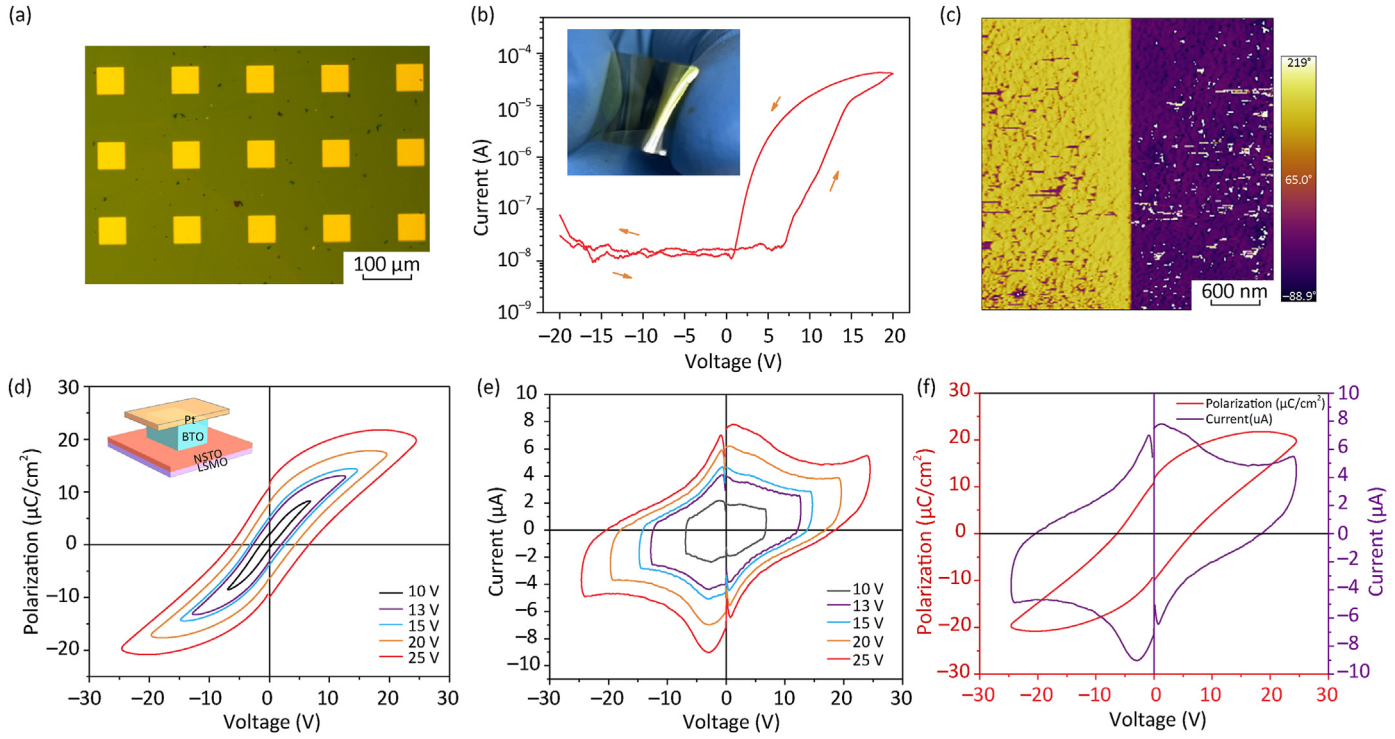

Fig. 3. A Pt/BTO/NSTO/LSMO/STO/Mica: (a) Optical image, (b) *I*–*V* curves with insert showing the photograph, (c) PFM phases for +25 V (left) and −25 V (right), (d) *P*–*V* hysteresis loops under 1 kHz conditions, (e) corresponding switching current curves, and (f) *P*–*V* circuit and corresponding switching current curve under 1 kHz conditions.

polarization. The polarization current curve confirmed once again the ferroelectricity of the epitaxial BTO thin film on a flexible mica, which was consistent with previous reports [39,41]. Subsequently, Fig. 3f shows the correlation between the polarization and the corresponding switching current. The coercive field, as indicated in the *P*–*V* loop, aligned with the transverse axis at the peak of the polarization current. The analysis did not only confirm the current transitions in the *I*–*V* curves, but also showed that the flexible Pt/BTO/NSTO/LSMO/STO/Mica device maintained favorable ferroelectric properties.

3.3. BTO ferroelectricity on flexible and rigid substrates

STO substrates are commonly used because of their strong structural conformity, which significantly affects the epitaxial alignment and subsequent ferroelectric properties of BTO films [22]. To align with the complementary metal oxide semiconductor (CMOS) fabrication regime, it has been reported that a deposition of a buffer layer on a Silicon (Si) substrate can reduce the lattice mismatch, thus improving the epitaxy of the BTO thin film [7]. These observations underscore the inherent complexities in the growth of BTO ferroelectric films. They also suggest the potential for diversifying the substrate, specifically by using mica as a viable option. As can be seen in Fig. 4, the device that was composed of Pt/BTO/NSTO/LSMO/STO layers grown on different substrates demonstrated the advantages of thin flexible substrates. The typical hysteresis curve for the mica substrate is shown in Fig. 4a. The residual polarization ($2P_r$ = 13.852 μC/cm^2) and maximum polarization ($2P_{max}$ = 33.805 μC/cm^2) revealed a good ferroelectricity of the flexible substrate. The $2P_{max}$ value for the film on an STO substrate was approximately 34.477 μC/cm^2, and the $2P_r$ value was close to 11.807 μC/cm^2 (Fig. 4b). This was accompanied by a coercive field of approximately 148.854 kV/cm. Fig S8 Supplementary information shows the *P*–*V* hysteresis loops for different substrates. The significant advantage of the flexible substrates was sufficient to compensate for the slight performance difference with respect to the STO substrates.

Furthermore, Fig. 4c illustrates the comparative indices that were used to assess the ferroelectric performance of the different substrate configurations. The coercivity field of the device on the rigid substrate was 148.85 kV/cm, and that of the device on the mica substrate was 189.393 kV/cm. Also, the mica substrate showed a larger coercive electric field. The $2P_r$ value of the device on the mica substrate (~13.852 μC/cm^2) was even higher than that of the device on the STO substrate (11.807 μC/cm^2). In addition, there were very similar $2P_{max}$ values. Notably, the flexible Pt/BTO/NSTO/LSMO/STO/Mica device had a favorable ferroelectricity, which was comparable to its counterparts formed on rigid substrates.

3.4. Device flexibility and durability

To investigate the durability and functional reliability of flexible devices, a wide range of bending tests have been conducted. These tests included devices that were unbent, bent to a specific curvature, and that had been undergoing 1000 cycles of bending. The photograph of a bending radius of 6 mm is presented in Fig. 5a. The schematic diagram of the precision bending equipment that repeatedly bent the devices is shown in Fig. 5b. Such convex deformation in the substrate induced a tensile stress across the surface of the film, which caused an axial elongation known as a tensile strain. For electronic devices, the interactions between the mechanical and electrical properties of the flexible ferroelectric thin film were crucial, particularly when assessing their performance under bending stress [37]. Hussain *et al.* presented a theoretical framework that addressed mechanical stress in relation to a specific nominal strain [32].

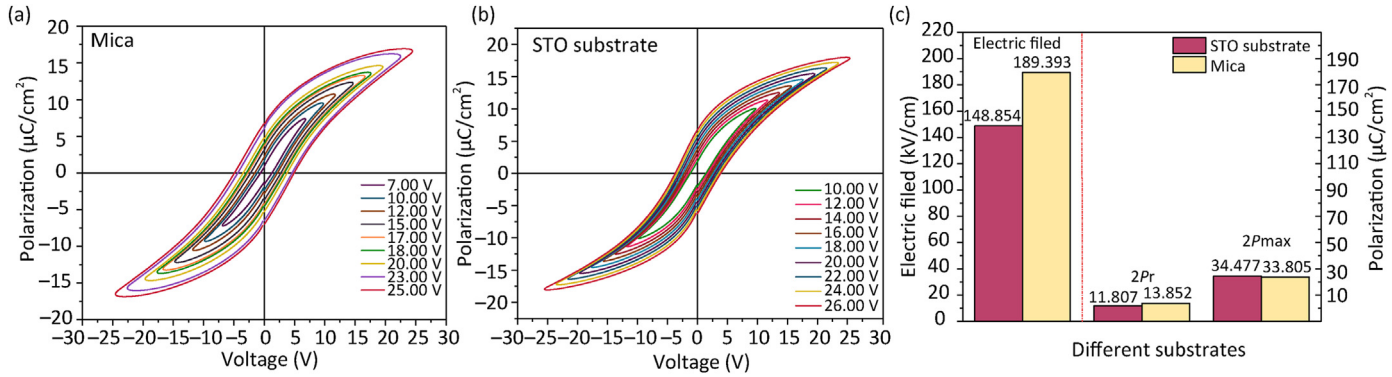

Fig. 4. (a) *P*–*V* hysteresis loops of Pt/BTO/NSTO/LSMO/STO/Mica under 1 kHz conditions, (b) *P*–*V* hysteresis loops of Pt/BTO/NSTO/LSMO/STO under 1 kHz conditions, and (c) a performance comparison chart of heterojunctions on different substrates.

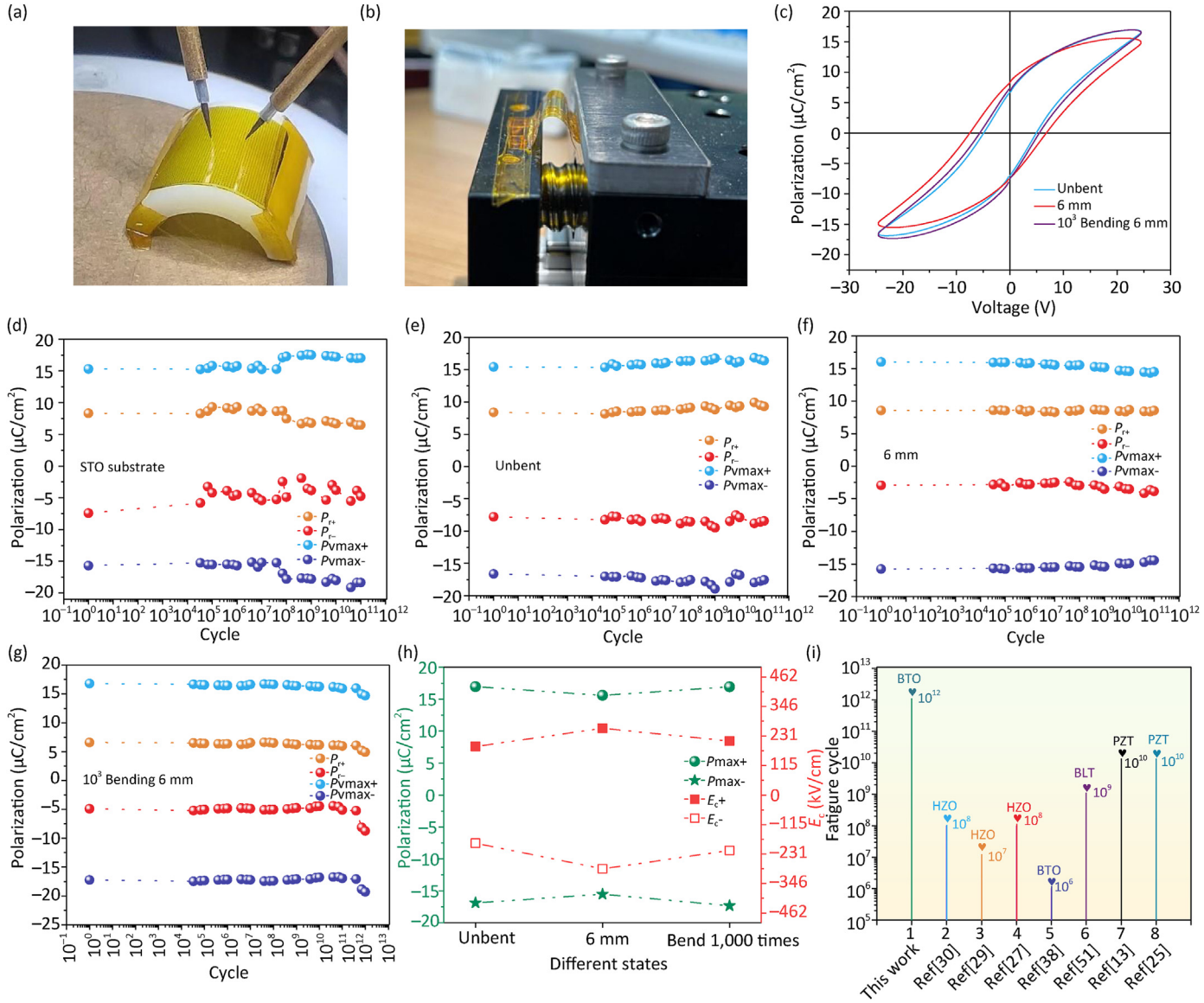

Fig. 5. (a) A 6 mm bending test image. (b) Mechanically repeated bending diagram. (c) *P*–*V* hysteresis loops for three different bending states. (d) Fatigue resistance testing of a rigid STO substrate at 100 kHz. Fatigue resistance testing of a mica substrate (e) in an unbent state at 100 kHz, (f) in a 6 mm bending state at 100 kHz, and (g) after 1000 bending cycles at 100 kHz. (h) *P*max and coercive electric field (E_C) values for various bending states (unbent, 6 mm bending, and 6 mm bending 1000 times). (i) Fatigue cycle resistance testing of inorganic ferroelectric thin films.

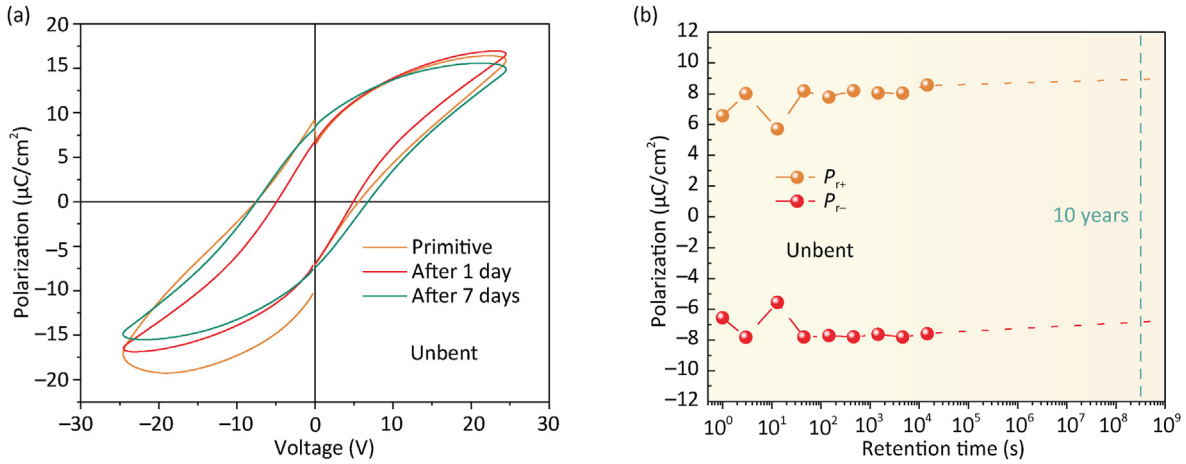

Fig. 6. (a) *P*–*V* hysteresis loops and (b) retention performance of Pt/BTO/NSTO/LSMO/STO/Mica.

$$\varepsilon_{\text{nominal}} = \frac{t}{2R} \quad (1)$$

where t represents the thickness and R is the bending radius. It is widely known that increased stress can lead to negative consequences, such as the onset of film cracking [37]. The exerted stress is directly proportional to the thickness of the film and inversely proportional to the radius of the curvature. Therefore, the stress can be reduced by either decreasing the thickness of the mica substrate, or by increasing the bending radius to a larger extent [32,43].

To investigate the durability of data storage applications, Fig. 5c illustrates the hysteresis loops of these devices under various conditions. A significant difference was observed in both the coercive field and the polarization level when going from an unbent state to a 6 mm bent state. The $2P_r$ reached its maximum value (~16.11 μC/cm^2) after being bent, which was an increase by ~2.15 μC/cm^2 compared with the unbent state. By contrast, the $2P_{max}$ value for the bent state was ~31.09 μC/cm^2, which was a slight decrease by ~2.71 μC/cm^2 compared with the unbent state. The small changes in polarization values were similar to those presented previously [25]. These variations within the defined tolerances indicated the robustness of the device during mechanical deformation. There is only a minimal change in the polarization values between the two conditions (unbent and bending 1000 times). The minimal changes in polarization due to deformation could be explained by the following. The ferroelectricity of ferroelectric thin films originated usually from the distortion of the internal lattice. The deformation of the BTO crystal occurred when external stresses were applied, which usually led to a change in the dielectric constant or polarization. When the bent state was restored to the unbent state, the polarization values also showed some recovery. These results were demonstrated in the study of Chu *et al.* [43]. This resilience reinforced the structural integrity of the device, demonstrating its ability to withstand stress-induced disturbances. The results showed that the prepared flexible BTO ferroelectric film in the present study, which was prepared on a mica substrate, exhibited an improved ferroelectricity.

The fatigue endurance of these devices under different mechanical strain conditions has also been investigated. Fig. 5d–g illustrates the fatigue characteristics that were observed under different bending scenarios. All fatigue tests were conducted using square (SQU) waveforms with a frequency of 100 kHz. Fig. 5d shows the stability of the devices on STO substrates. It was found that the $2P_r$ value decreased slightly after 10^{11} cycles, while the $2P_{max}$ value showed a minor increase. The $2P_r$ value decreased from 15.75 μC/cm^2 to 11.24 μC/cm^2, which was a decrease of 4.51 μC/cm^2. The $2P_{max}$ value increased from 30.99 μC/cm^2 to 35.37 μC/cm^2, with an increase of 4.38 μC/cm^2. Notably, there were also polarization fluctuations near 10^8 cycles, which could be attributed to the internal redistribution of oxygen vacancies within the BTO film as the cycle number increased. Furthermore, the data indicated that the Pt/BTO/NSTO/LSMO devices on STO substrates had a certain instability.

Fig. 5e presents the fatigue resistance of unbent flexible Pt/BTO/NSTO/LSMO/STO/Mica devices. These devices showed the ability to sustain stability over 10^{11} cycles, with minimal increases in both the remaining polarization and the maximum polarization. The $2P_r$ value increased from 16.19 μC/cm^2 to 17.74 μC/cm^2, with an increase of 1.552 μC/cm^2. The $2P_{max}$ value increased from 32.064 μC/cm^2 to 33.93 μC/cm^2, with an increase of 1.87 μC/cm^2. The slight changes in polarization values demonstrated the high stability of the flexible heterojunction devices. This was an indication of an excellent fatigue resistance of the flexible substrates when compared with those on the STO substrate.

Furthermore, when the flexible device went from unbent to a bending radius of 6 mm, there was a significant increase in the coercive field (Fig. 5f). After 10^{11} bipolar switching cycles, the polarization value of the flexible heterojunction device slightly changed. It increased from 11.50 μC/cm^2 to 12.42 μC/cm^2, and the $2P_{max}$ decreased from 31.79 μC/cm^2 to 28.94 μC/cm^2. The flexible device was also subject to 1000 repeated bending cycles with a bending radius of 6 mm, and the results from the durability test is presented in Fig. 5g. It was observed that after 10^{12} cycles, there was a slight change in the polarization value. The $2P_r$ value increased from 11.48 μC/cm^2 to 13.63 μC/cm^2, and the $2P_{max}$ value decreased from 34.03 μC/cm^2 to 33.91 μC/cm^2. The above-presented data showed that this flexible BTO ferroelectric film proved to be suitable for flexibility in a non-volatile memory (NVM).

The metrics of the maximum P_{max} and E_c have also been evaluated (Fig. 5h). After transferring from the unbent state to the fixed 6 mm bent state, the increase in the coercive electric field and the decrease in the polarization value could be ascribed to the stresses induced in the bent configuration. These results were aligned with prior research findings [29]. Furthermore, the polarization value and coercive field of the device reverted to the unbent state after 1000 bends, which were a marginal reduction and increment, respectively. However, this reversion was significantly less pronounced than under fixed bending. Thus, it was assumed that this phenomenon originated from the resistance variation induced by

the tensile stresses that arose from bending. Furthermore, the fixed 6 mm bending caused a more substantial resistance shift than the multiple bending. The above-presented results demonstrated that there was no notable performance change in the flexible devices under bending conditions, which was similar to previous reports [32].

The fatigue tests of flexible Pt/BTO/NSTO/LSMO/STO/Mica devices under two bending conditions showed lower performance change rates, which proved that the here prepared Pt/BTO/NSTO/LSMO/STO/Mica flexible devices had a good stability. Fig. 5i compares the endurance cycles for different ferroelectric materials, which have been reported in recent years. A comparative analysis of the flexible HZO ferroelectric memory and flexible memories based on BTO, PZT, and BLT thin films showed instability after 10^9 cycles. The flexible HZO ferroelectric memory showed significant fatigue after 10^6 cycles. However, the results in the present study have revealed stability that extends up to 10^{12} cycles [25,29,30,32,39,51]. This observation verified the exemplary ferroelectric durability of flexible Pt/BTO/NSTO/LSMO/STO/Mica devices, which were fabricated using a pulsed laser deposition system. This extraordinary ferroelectricity was obtained for various bending states and compared with the rigid STO substrate.

Furthermore, the retention characteristics of the heterojunction in the unbent state are shown in Fig. 6. The flexible ferroelectric BTO thin film still exhibited excellent ferroelectricity after being stored for a period (Fig. 6a). Also, at a pulse width of 10 ms, the device could still maintain excellent retention characteristics after 10^4 s (Fig. 6b), and the retention time of the polarization state may reach up to 10 years. In the ultra-thin BTO FTJ, the high and low resistance states exhibit stable retention characteristics within 300 s, as shown in Fig. S9 Supplemental information. These results confirm that flexible BTO ferroelectric thin films have excellent retention properties.

4. Conclusions

In this study, (111)-oriented flexible BTO ferroelectric thin films on mica substrates have been successfully prepared using a pulsed laser deposition system. The multi-layer thin film was proven to be heteroepitaxial by XRD and TEM analyses. The use of a multi-layer buffer layer enabled the Pt/BTO/NSTO/LSMO/STO/Mica flexible devices to exhibit excellent ferroelectricity (P_r~21.39 μC/cm^2, P_{max}~42.58 μC/cm^2). With no external electric field, the flexible device showed excellent retention characteristics for over 10^4 s. For 10^3 bending cycles with a bending radius of 6 mm, the structure exhibited the highest number of bipolar switching cycles (10^{12}) among all reported flexible ferroelectric thin films. Additionally, this study revealed significant changes in the ferroelectricity of the devices for a bending radius of 6 mm, which was caused by the influence of bending stress. These findings have demonstrated that Pt/BTO/NSTO/LSMO/STO/Mica flexible devices can be potentially used in the field of non-volatile memories.

CRediT authorship contribution statement

Xingpeng Liu: Supervision, Data curation. **Chunshu Wei:** Writing – original draft. **Tangyou Sun:** Conceptualization. **Fabi Zhang:** Funding acquisition. **Haiou Li:** Funding acquisition. **Linsheng Liu:** Data curation. **Ying Peng:** Writing – review & editing. **Hezhang Li:** Writing – review & editing. **Min Hong:** Validation.

Declaration of competing interests

The authors declare that they have no known competing financial interests or personal relationships that could have appeared to influence the work reported in this paper.

Acknowledgements

Project support by Guangxi Natural Science Foundation (NO.2023GXNSFBA026216), National Natural Science Foundation of China (NO.62361022, 52061009, 61964003, 52262022, 62174041).

Appendix A. Supplementary data

Supplementary data to this article can be found online at https://doi.org/10.1016/j.jmat.2024.04.001.

References

[1] Garcia V, Bibes M. Ferroelectric tunnel junctions for information storage and processing. Nat Commun 2014;5:4289.
[2] Gao W, Zhu Y, Wang Y, Yuan G, Liu J. A review of flexible perovskite oxide ferroelectric films and their application. J Materiomics 2020;6(1):1–16.
[3] Zheng H, Bai Y, Shao Y, Yu H, Chen B, Lin J, et al. Understanding and modulation of resistive switching behaviors in $PbZr_{0.52}Ti_{0.48}O_3/La_{0.67}Sr_{0.33}MnO_3$/Nb:$SrTiO_3$ multilayer junctions. Appl Surf Sci 2022;574:151711.
[4] Li C, Huang L, Li T, Lu W, Qiu X, Huang Z, et al. Ultrathin $BaTiO_3$-based ferroelectric tunnel junctions through interface engineering. Nano Lett 2015;15(4):2568–73.
[5] Ma C, Luo Z, Huang W, Zhao L, Chen Q, Lin Y, et al. Sub-nanosecond memristor based on ferroelectric tunnel junction. Nat Commun 2020;11(1):1439.
[6] Wang X, Song B, Tao LL, Wen J, Zhang L, Zhang Y, et al. Effect of a semiconductor electrode on the tunneling electroresistance in ferroelectric tunneling junction. Appl Phys Lett 2016;109(16).
[7] Wang T, Hsu P, Korytov M, Genoe J, Merckling C. Polarization control of epitaxial barium titanate ($BaTiO_3$) grown by pulsed-laser deposition on a MBE-$SrTiO_3$/Si(001) pseudo-substrate. J Appl Phys 2020;128(10):104104.
[8] Hou P, Gao Z, Ni K. Multilevel data storage memory based on polycrystalline $SrTiO_3$ ultrathin film. RSC Adv 2017;7(78):49753–8.
[9] Yang B, Li C, Liu M, Wei R, Tang X, Hu L, et al. Design of flexible inorganic $BiFe_{0.93}Mn_{0.07}O_3$ ferroelectric thin films for nonvolatile memory. J Materiomics 2020;6(3):600–6.
[10] Li D, Zhao P, Deng X, Wu Y, He X, Liu D, et al. A new organic–inorganic hybrid perovskite ferroelectric $[C_lCH_2CH_2N(CH_3)_3][PbBr_3]$ and its PVDF matrix-assisted highly-oriented flexible ferroelectric films. New J Chem 2022;46(40):19391–400.
[11] Kim A, Huseynova G, Lee J, Lee JH. Enhancement of out-coupling efficiency of flexible organic light-emitting diodes fabricated on an MLA-patterned parylene substrate. Org Electron 2019;71:246–50.
[12] Sun H, Luo Z, Zhao L, Liu C, Ma C, Lin Y, et al. $BiFeO_3$-based flexible ferroelectric memristors for neuromorphic pattern recognition. ACS Appl Electron Mater 2020;2(4):1081–9.
[13] Bakaul SR, Serrao CR, Lee O, Lu Z, Yadav A, Carraro C, et al. High speed epitaxial perovskite memory on flexible substrates. Adv Mater 2017;29(11):1605699.
[14] Luo Z, Peters JJP, Sanchez AM, Alexe M. Flexible memristors based on single-crystalline ferroelectric tunnel junctions. ACS Appl Mater Interfaces 2019;11(26):23313–9.
[15] Huang J, Chen W. Flexible strategy of epitaxial oxide thin films. iScience 2022;25(10):105041.
[16] Lu L, Dai Y, Du H, Liu M, Wu J, Zhang Y, et al. Atomic scale understanding of the epitaxy of perovskite oxides on flexible mica substrate. Adv Mater Interfac 2019;7(2):1901265.
[17] Lu Z, Liu J, Feng J, Zheng X, Yang L, Ge C, et al. Synthesis of single-crystal $La_{0.67}Sr_{0.33}MnO_3$ freestanding films with different crystal-orientation. Apl Mater 2020;8(5):051155.
[18] Nian L, Li J, Wang Z, Zhang T, Sun H, Li Y, et al. Synthesis of oxide interface-based two-dimensional electron gas on Si. ACS Appl Mater Interfaces 2022;14(47):53442–9.
[19] Lu D, Baek DJ, Hong SS, Kourkoutis LF, Hikita Y, Hwang HY. Synthesis of freestanding single-crystal perovskite films and heterostructures by etching of sacrificial water-soluble layers. Nat Mater 2016;15(12):1255–60.
[20] Xu R, Huang J, Barnard ES, Hong SS, Singh P, Wong EK, et al. Strain-induced room-temperature ferroelectricity in $SrTiO_3$ membranes. Nat Commun 2020;11(1):3141.
[21] Bakaul SR, Serrao CR, Lee M, Yeung CW, Sarker A, Hsu SL, et al. Single crystal functional oxides on silicon. Nat Commun 2016;7:10547.
[22] Chiabrera FM, Yun S, Li Y, Dahm RT, Zhang H, Kirchert CKR, et al. Freestanding perovskite oxide films: synthesis, challenges, and properties. Ann Phys 2022;534(9):2200084.
[23] Ji D, Cai S, Paudel TR, Sun H, Zhang C, Han L, et al. Freestanding crystalline oxide perovskites down to the monolayer limit. Nature 2019;570(7759):87–90.
[24] Zhao Z, Abdelsamie A, Guo R, Shi S, Zhao J, Lin W, et al. Flexible artificial synapse based on single-crystalline $BiFeO_3$ thin film. Nano Res 2021;15(3):

2682–8.
[25] Jiang J, Bitla Y, Huang C, Do T, Liu H, Hsieh Y, et al. Flexible ferroelectric element based on van der waals heteroepitaxy. Sci Adv 2017;3(6):e1700121.
[26] Mo S, Feng K, Pang J, Ouyang K, Jiang L, Yang Q, et al. All-inorganic transparent $Hf_{0.85}Ce_{0.15}O_2$ ferroelectric thin films with high flexibility and stability. Nano Res 2022;16(4):5065–72.
[27] Chen Y, Yang Y, Yuan P, Jiang P, Wang Y, Xu Y, et al. Flexible $Hf_{0.5}Zr_{0.5}O_2$ ferroelectric thin films on polyimide with improved ferroelectricity and high flexibility. Nano Res 2021;15(4):2913–8.
[28] Zhou X, Sun H, Li J, Du X, Wang H, Luo Z, et al. A flexible $Hf_{0.5}Zr_{0.5}O_2$ thin film with highly robust ferroelectricity. J Materiomics 2023;10(1):210–7.
[29] Joh H, Jung M, Hwang J, Goh Y, Jung T, Jeon S. Flexible ferroelectric hafnia-based synaptic transistor by focused-microwave annealing. ACS Appl Mater Interfaces 2022;14(1):1326–33.
[30] Liu H, Lu T, Li Y, Ju Z, Zhao R, Li J, et al. Flexible quasi-van der waals ferroelectric hafnium-based oxide for integrated high-performance nonvolatile memory. Adv Sci 2020;7(19):2001266.
[31] Liu W, Liao J, Jiang J, Zhou Y, Chen Q, Mo S, et al. Highly stable performance of flexible $Hf_{0.6}Zr_{0.4}O_2$ ferroelectric thin films under multi-service conditions. J Mater Chem C 2020;8(11):3878–86.
[32] Xiao W, Liu C, Peng Y, Zheng S, Feng Q, Zhang C, et al. Thermally stable and radiation hard ferroelectric $Hf_{0.5}Zr_{0.5}O_2$ thin films on muscovite mica for flexible nonvolatile memory applications. ACS Appl Energy Mater 2019;1(6):919–27.
[33] Zhong H, Li M, Zhang Q, Yang L, He R, Liu F, et al. Large-scale $Hf_{0.5}Zr_{0.5}O_2$ membranes with robust ferroelectricity. Adv Mater 2022;34(24):e2109889.
[34] Silva A, Fina I, Sánchez F, Silva JPB, Marques L, Lenzi V. Unraveling the ferroelectric switching mechanisms in ferroelectric pure and La doped HfO_2 epitaxial thin films. Mater Today Phys 2023;34:101064.
[35] Yang Y, Yuan G, Yan Z, Wang Y, Lu X, Liu J. Flexible, semitransparent, and inorganic resistive memory based on $BaTi_{0.95}Co_{0.05}O_3$ Film. Adv Mater 2017;29(26):1700425.
[36] Hou P, Yang K, Ni K, Wang J, Zhong X, Liao M, et al. An ultrathin flexible electronic device based on the tunneling effect: a flexible ferroelectric tunnel junction. J Mater Chem C 2018;6(19):5193–8.
[37] Liu J, Feng Y, Tang R, Zhao R, Gao J, Shi D, et al. Mechanically tunable magnetic properties of flexible $SrRuO_3$ epitaxial thin films on mica substrates. Adv Electron Mater 2018;4(4):1700522.
[38] Wu J, Liang Z, Ma C, Hu G, Shen L, Sun Z, et al. Flexible lead-free $BaTiO_3$ ferroelectric elements with high performance. IEEE Electron Device Lett 2019;40(6):889–92.
[39] Yang C, Han Y, Qian J, Cheng Z. Flexible, temperature-stable, and fatigue-endurable $PbZr_{0.52}Ti_{0.48}O_3$ ferroelectric film for nonvolatile memory. Adv Electron Mater 2019;5(10):1900443.
[40] An F, Zi M, Chen Q, Liu C, Qu K, Jia T, et al. Flexible room-temperature multiferroic thin film with multifield tunable coupling properties. Mater Today Phys 2022;23:100615.
[41] Chen Q, Zhang Y, Tang M, Yang L, Zhong X, Ren C, et al. Significantly enhanced energy storage density and efficiency in flexible $Bi_{3.15}Nd_{0.85}Ti_3O_{12}$ thin film via periodic dielectric layers. J Appl Phys 2022;131(11):114101.
[42] Sun H, Luo Z, Liu C, Ma C, Wang Z, Yin Y, et al. A flexible $BiFeO_3$-based ferroelectric tunnel junction memristor for neuromorphic computing. J Materiomics 2022;8(1):144–9.
[43] Ko DL, Tsai MF, Chen JW, Shao PW, Tan YZ, Wang JJ, et al. Mechanically controllable nonlinear dielectrics. Sci Adv 2020;6(10):eaaz3180.
[44] Wen Z, Wu D. Ferroelectric tunnel junctions: modulations on the potential barrier. Adv Mater 2020;32(27):e1904123.
[45] Wen Z, Li C, Wu D, Li A, Ming N. Ferroelectric-field-effect-enhanced electroresistance in metal/ferroelectric/semiconductor tunnel junctions. Nat Mater 2013;12(7):617–21.
[46] Yang Y, Wu M, Li X, Hu H, Jiang Z, Li Z, et al. The role of ferroelectric polarization in resistive memory properties of metal/insulator/semiconductor tunnel junctions: acomparative study. ACS Appl Mater Interfaces 2020;12(29):32935–42.
[47] Li D, Zhu X, Wu Y, Zhao J, Zhang K, Li R, et al. La-doped $BiFeO_3$ junction based random access multilevel nonvolatile memory. Microelectron Eng 2023;267–268:111908.
[48] Du X, Sun H, Wang H, Li J, Yin Y, Li X. High-speed switching and giant electroresistance in an epitaxial $Hf_{0.5}Zr_{0.5}O_2$-based ferroelectric tunnel junction memristor. ACS Appl Mater Interfaces 2022;14(1):1355–61.
[49] Shin W, Yim J, Bae JH, Lee JK, Hong S, Kim J, et al. Synergistic improvement of sensing performance in ferroelectric transistor gas sensors using remnant polarization. Mater Horiz 2022;9(6):1623–30.
[50] Yu H, Chung CC, Shewmon N, Ho S, Carpenter JH, Larrabee R, et al. Flexible inorganic ferroelectric thin films for nonvolatile memory devices. Adv Funct Mater 2017;27(21):1700461.
[51] Su L, Lu X, Chen L, Wang Y, Yuan G, Liu JM. Flexible, fatigue-free, and large-scale $Bi_{3.25}La_{0.75}Ti_3O_{12}$ ferroelectric memories. ACS Appl Mater Interfaces 2018;10(25):21428–33.

Xingpeng Liu is currently a associate professor in Guilin University of Electronic Technology. He obtained his Ph.D. degree of Engineering degree from the National Key Laboratory of Electronic Thin Films and Integrated Devices at the University of Electronic Science and Technology of China in 2018. He has been engaged in research in the field of micro-nano sensors and high electron mobility transistors (HEMT) for many years.

Ying Peng received a Ph.D. degree from Nagoya University, Japan. He is currently working as a professor in Guilin University of Electronic Technology. His research interests include silicon-germanium based thermoelectric materials and devices, germanium based phase-change memory, and other thin-film electronic devices.

Hezhang Li received his Ph.D. degree from Tohoku University, Japan in 2022 and then worked in National Institute for Materials Science (NIMS), Japan as a postdoc researcher from April 2022 to February 2023. He is now a postdoctoral researcher at Tsinghua University, China. His research focuses on the calculation of electronic structure, crystal structure analysis and the transport properties of Heusler alloys and other semiconductor materials.

Min Hong received a Ph.D. degree from the University of Queensland. Currently, he is an associate professor and ARC future fellow at University of Southern Queensland, Australia. His research focuses on thermoelectric technology, including semiconductor thermoelectric materials, organic/inorganic flexible thermoelectrics, physical/chemical principles of transport properties, and thermoelectric devices for refrigeration and power generation.